Photocatalytic activity of TiO$_2$-WO$_3$ mixed oxides in relation to electron transfer efficiency

Maria Vittoria Dozzi [a,*], Stefania Marzorati [a], Mariangela Longhi [a], Mauro Coduri [b], Luca Artiglia [c], Elena Selli [a]

[a] Dipartimento di Chimica, Università degli Studi di Milano, via Golgi 19, I-20133 Milano, Italy
[b] CNR-IENI Institute for Energetics and Interphases, C.so Promessi Sposi 29, I-23900 Lecco, Italy
[c] Dipartimento di Scienze Chimiche, Università degli Studi di Padova, via Marzolo 1, I-35131 Padova, Italy

ABSTRACT

Aiming at producing photocatalysts with minimized photoproduced electron – hole pairs recombination, a series of titanium – tungsten mixed oxides has been prepared, by coupling TiO$_2$ with different amounts of WO$_3$, according to an alkaline-catalyzed sol-gel method followed by an incipient wetting procedure. The photocatalysts were characterized by surface and bulk techniques and tested in both an oxidation and a reduction photocatalytic reaction, *i.e.* in formic acid (FA) mineralization and in Cr(VI) reduction. Tungsten was mainly present as hexagonal WO$_3$ on the TiO$_2$ surface, though a fraction of W migrates into the TiO$_2$ lattice substituting Ti atoms, as evidenced by XRPD analysis. Different photoactivity scales were found in the two test reactions, both occurring in the same pH range under similar substrate-photocatalyst electrostatic interactions. In fact, photoexcited electrons transferred from the conduction band (CB) of TiO$_2$ to the CB of coupled WO$_3$, being energetically unable to reduce O$_2$ molecules, easily recombine with photoproduced holes, with a consequent photoactivity decrease in FA photo-mineralization with increasing W/Ti ratio. On the contrary, coupling TiO$_2$ with small WO$_3$ amounts (0.2–1.0 mol%) is beneficial in the removal of Cr$_2$O$_7^{2-}$ anions. These species, being characterized by a redox potential more positive than the CB edge of WO$_3$, may efficiently accept the electrons trapped in WO$_3$ domains, converting into less toxic Cr(III) species. Thus, WO$_3$ surface domains effectively promote photoproduced charge separation by efficiently trapping CB electrons; increased photocatalytic efficiency depends on the redox potential of the electron acceptor species directly (or indirectly) involved in the photocatalytic process.

© 2016 Elsevier B.V. All rights reserved.

1. Introduction

Many strategies have been employed in the last decade in order to minimize a crucial drawback of TiO$_2$ use as photocatalytic material, *i.e.* the fast and undesired recombination of photoproduced electron – hole pairs, strongly limiting the overall efficiency of photocatalytic processes occurring on the oxide surface [1,2]. In particular, besides the well-established effects in photogenerated electron-hole separation induced by surface noble metal (Au, Pt) nanoparticles able to capture conduction band electrons [3,4], the idea of coupling TiO$_2$ with another metal oxide with suitable band gap and edge positions can be pursued as a possible route to enhance photoproduced charge separation [5,6]. In fact, by coupling TiO$_2$ with a metal oxide having the conduction band (CB) lower in energy than the CB of TiO$_2$, photopromoted electrons may transfer from the CB of TiO$_2$ to that of the other metal oxide, while photogenerated holes remain trapped within the TiO$_2$ particles, with consequent increased electron-hole separation. Among the possible semiconductor metal oxides, crystalline WO$_3$ has a suitable CB energy which enables electrons photopromoted in the CB of TiO$_2$ to transfer into the CB of WO$_3$ [5].

TiO$_2$/WO$_3$ nanocomposites, prepared by different techniques, including sol-gel [7–9], impregnation [10,11], hydrothermal reaction [12], ball milling [13], flame spray synthesis [14], and in different forms [15–17] were mainly used in the photocatalytic degradation of organic pollutants also under possible visible light activation [7,15]. Unfortunately, most of these studies employed dyes as degradation substrates [7–9,11,12,14,16], which makes the interpretation of the photoactivity results rather controversial, due to the possible dye-sensitized path parallel to photocatalyst activation, charge separation and charge transfer at the photocatalyst surface [18].

In general, the increased photocatalytic activity observed upon tungsten addition to TiO_2 was ascribed to increased charge separation efficiency [19], though other effects also need to be invoked, such as the increased surface acidity consequent to WO_3 introduction, which may alter the surface charge and thus the substrate adsorption equilibria [10,14], and the increased surface area of the W-modified material, consequent to the stabilized anatase phase upon doping TiO_2 with W and leading to increased absorption capacity of the doped materials [8,11].

In the present work we systematically investigate the effects on photoactivity induced by modifying TiO_2 with different amounts of WO_3 in TiO_2-WO_3 mixed oxides. This study follows a previous investigation on the same mixed oxides [20] prepared by sol-gel synthesis starting from alkoxide solutions of the two metals, which left open the question if the superior performance of these mixed oxide photocatalysts should be ascribed to the presence of separate domains of the two oxides, or simply be a consequence of W-doping of TiO_2. For this reason, in the present work the photocatalytic materials were prepared starting from pure titania, followed by its surface modification by different amounts of WO_3. The so obtained mixed oxides photocatalysts were tested in both an oxidation and a reduction photocatalytic reaction, *i.e.* in formic acid (FA) mineralization and in Cr(VI) reduction. The fact that both reactions occur in aqueous suspension at pH 3.7 starting from negatively charged substrates makes the comparison between the photoactivity of the TiO_2-WO_3 photocatalysts much easier, any effect related to different pH conditions being avoided.

In fact, the pH of aqueous suspensions may strongly affect the charging process of −OH groups exposed on the photocatalyst surface which may act as specific adsorption sites for the photocatalytically transformed species. Indeed, the here chosen test compounds (*i.e.* formate and dichromate anions) are both negatively charged, so they have similar affinity for the investigated photocatalysts surface in the same pH range.

Formic acid (FA) is an excellent photodegradation substrate to preliminarily check photoactivity because it does not absorb in the UV–vis region and it undergoes direct photomineralization without forming any stable intermediate species, which simplifies the interpretation of kinetic results. Though not being a pollutant, FA can be envisaged as a model substrate of the oxidative degradation of organic species mainly occurring through direct interaction with the holes photoproduced in the semiconductor photocatalyst system.

On the other hand, Cr(VI) ions, which are notoriously toxic and carcinogenic, are generally released in effluents by various industrial activities (*e.g.* electroplating, leather tanning, textile production, steel fabrication). The development of materials able to efficiently promote their photocatalytic reduction has great importance in the scenario of photocatalysis as innovative and clean technology for industrial wastewaters decontamination.

2. Experimental

2.1. Photocatalysts preparation

Amorphous TiO_2, labeled as P, was synthesized according to an alkaline-catalyzed sol-gel method, as follows. Titanium isopropoxide (40 mL) was mixed with 2-propanol (50 mL) and the so obtained solution was vigorously stirred for 15 min. Then 250 mL of a 15 mM aqueous KOH solution were added dropwise to the titanium-containing solution. Hydrolysis occurred immediately. After stirring for 90 min at room temperature, the obtained white slurry was centrifuged, washed twice with freshly distilled water, dried in air at 80 °C for 24 h and finally ball-milled for 5 min at 10 Hz.

The series of TiO_2-WO_3 mixed oxides was prepared by an incipient wetting procedure, as follows. An aqueous solution (3 mL) containing the proper amount of ammonium *meta*-tungstate hydrate, $(NH_4)_6H_2W_{12}O_{40} \cdot xH_2O$, was added dropwise to 1.5 g of P, in order to obtain W/Ti nominal percent molar ratios in the 0.2–3.0 range. The slurry was mildly stirred for 24 h, then dried in air at 120 °C for 24 h and ball-milled for 5 min at 10 Hz. The resulting powder was annealed in air at 450 °C for 24 h, with an initial heating ramp of 7 °C min^{-1}.

The so obtained samples were labeled as T_W(X), with X referring to the nominal W/Ti percent molar ratio. Samples prepared with W/Ti = 5.0% were mainly used for XRPD characterization. They were calcined either at 450 °C or at 600 °C for 24 h and labeled as Ti_W(5) and Ti_W(5)_600, respectively. Moreover reference TiO_2 samples, labeled as T and T_600, were prepared by following exactly the same synthetic route in the absence of any W precursor, followed by thermal treatment at 450 °C or 600 °C for 24 h, respectively. Finally a bare WO_3 powder, labeled as W, was obtained by annealing a batch of solid ammonium *meta*-tungstate hydrate at 450 °C for 24 h.

All chemicals employed in the synthesis of the materials and in the preparation of the solutions were purchased from Aldrich. Water purified by a Milli-Q water system (Millipore) was used throughout.

2.2. Photocatalysts characterization

The BET specific surface area (SSA) of the materials was measured by N_2 adsorption/desorption at liquid nitrogen temperature in a Micromeritics Tristar II 3020 V1.03 apparatus, after out-gassing at 300 °C for 1 h under N_2 stream. Diffuse reflectance (DR) spectra of the photocatalyst powders were recorded with a Jasco V-670 spectrophotometer equipped with a PIN-757 integrating sphere, using barium sulphate as reference, and then converted into absorption (A) spectra (A = 1−R).

X-ray photoelectron spectroscopy (XPS) data were collected in a multi-technique ultra-high-vacuum (UHV) chamber (base pressure: 1.0×10^{-9} mbar) equipped with a VG MKII ESCALAB electron analyzer (5 channeltrons). XPS spectra were collected at room temperature in normal emission using a non monochromatized Mg anode X-ray source ($h\nu$ = 1253.6 eV). The calibration of the binding energy (BE) scale was determined using the Ti $2p_{3/2}$ maximum as reference. Powder samples were suspended in bi-distilled water and drop-casted on high-purity copper foils. After drying in air, the obtained films were introduced into the UHV chamber and outgassed overnight. The charging observed during measurements was corrected by aligning the Ti $2p_{3/2}$ core-level peak signal to 459.0 eV.

Energy dispersive X-ray (EDX) spectroscopy experiments, performed using a Zeiss Leo 1430 Scanning Electron Microscope equipped with an Energy Dispersive Spectroscopic (EDS) microanalysis probe from Oxford instruments, provided information on the composition of the photocatalysts, in terms of atomic percent amounts.

X-ray powder diffraction (XRPD) patterns were recorded at the ID22 beamline of the ESRF (European Synchrotron Radiation Facility, Grenoble) at room temperature with an incident wavelength λ = 0.31992 Å, up to 2θ = 50°. The powdered samples were packed into 1.0 mm in diameter kapton capillaries and were spun during data collection. The patterns were analyzed employing the Rietveld refinement, as implemented in the GSAS software [21]. Patterns were corrected for anomalous scattering and for absorption through the Lobanov formula [22], after direct determination of the packing fraction of the powder into the capillary. The distribution of W ions within the anatase phase was determined by refining the atomic Ti/W occupation factor of the 4b site (0, ¼, 3/8)

of anatase during the last refinement cycles. The average crystallite size was estimated by the Williamson-Hall analysis [23].

The point of zero charge (pH$_{pzc}$) of the main photocatalysts was determined by the mass titration method, which is based on the measurement of the limiting pH value obtained by adding small amounts of semiconductor powder in a supporting electrolyte solution [24]. Before each pH$_{pzc}$ determination all glasswares were washed with concentrated HCl (37%) and H$_2$SO$_4$ (98%) and the pH-meter was calibrated against two standard solutions. A saturated calomel reference electrode (Ingold), placed in an external compartment, was connected to the electrochemical cell in which a glass pH electrode without alkaline error (Metrohm 6.0150.100) was immersed. 30 mL of a 1.0×10^{-2} M LiNO$_3$ aqueous solution were added to the cell and degassed for 1 h under a nitrogen stream. Then, small amounts (5–15 mg) of photocatalyst were added to the electrolyte solution under stirring and the corresponding pH value was measured after equilibration. This procedure was repeated until the pH of the suspension did not significantly change after further addition of semiconductor powder. The so obtained plateau pH value was taken as pH$_{pzc}$ value of the investigated material.

2.3. Photoactivity tests

2.3.1. Photocatalytic decomposition of formic acid

All photocatalytic formic acid (FA) degradation runs were performed under atmospheric conditions in a magnetically stirred 60 mL cylindrical quartz reactor, inserted in a home made housing consisting of a black box mounted on optical bench [3]. The irradiation source was an Osram, model Powerstar HCI-T, 150 W/NDL lamp, mounted on a Twin Beam T 150 R reflector, emitting at $\lambda_{em} > 340$ nm, with an average full emission intensity on the reactor of 90 mW cm^{-2} as regularly checked with an optical power meter (Thorlabs PM200) equipped with a Thorlabs S130VC photodiode with silicon detector.

The irradiated aqueous suspensions always contained 0.1 g L^{-1} of photocatalyst and a FA initial concentration equal to 1.0×10^{-3} mol L^{-1}. After preliminary ultrasound treatment for 30 min, the suspension was magnetically stirred in the dark for 15 min to attain the adsorption equilibrium of the substrate on the photocatalyst surface, before starting irradiation. Stirring was continued during the photocatalytic runs. 2 mL-samples of the suspension were withdrawn from the photoreactor at different time intervals during the runs and centrifuged employing an EBA-20 Hettich centrifuge. The supernatant was analyzed for residual FA content by ion chromatography with conductivity detection, employing a Metrohm 761 Compact IC instrument, after calibration for formate ion concentration in the 0–50 ppm range. During FA degradation the pH of the suspensions increased, from initial values around 3.7 to ca. 4.8, as a consequence of FA mineralization to CO$_2$ and H$_2$O.

2.3.2. Cr(VI) photocatalytic reduction

All photocatalytic runs were performed in aqueous suspensions under atmospheric conditions, in a magnetically stirred 100 mL reactor, inserted in the previously described set-up [25]. All irradiated and pre-sonicated suspensions contained 0.1 g L^{-1} of photocatalyst and an initial Cr(VI) concentration equal to 3.3×10^{-5} mol L^{-1}, obtained by dissolving K$_2$Cr$_2$O$_7$ in water. The initial pH of the suspensions was fixed at 3.7 by addition of an appropriate volume of a concentrated HClO$_4$ solution. The adsorption equilibrium of the inorganic substrate was attained under magnetic stirring for 15 min in the dark. Stirring was continued during irradiation. At different time intervals during the runs, 3-mL samples of the suspension were withdrawn from the reactor and centrifuged. The supernatant was analyzed colorimetrically for Cr(VI) residual content, using the 1,5-diphenylcarbazide method
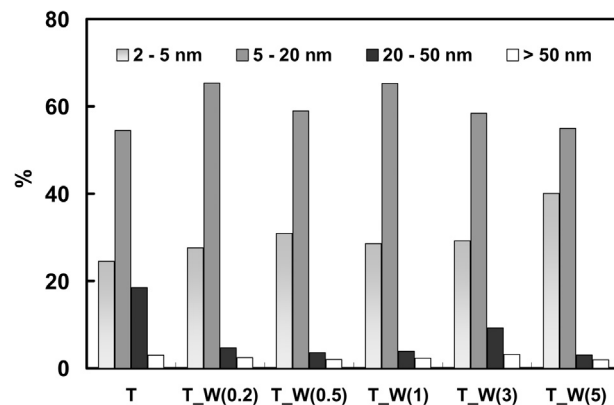

Fig. 1. Pore size range distribution obtained by the Barrett–Joyner–Halenda (BJH) analysis of the N$_2$ desorption isotherms of the investigated photocatalysts.
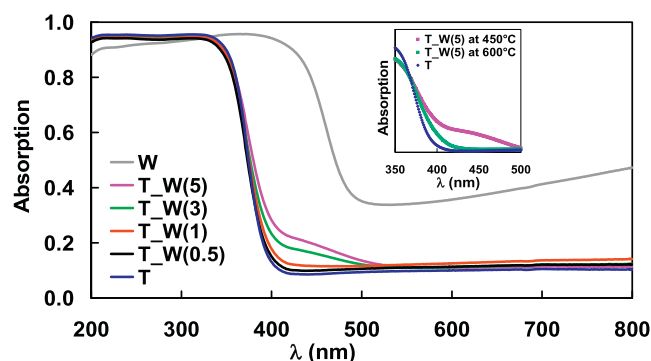

Fig. 2. UV–vis absorption spectra of pure TiO$_2$ (T), WO$_3$ (W) and T_W(X) (X = 0.5, 1, 3, 5). The effect induced on the absorption spectrum of T_W(5) by a calcination temperature increase from 450 to 600 °C is highlighted in the inset.

[26]. In this case no significant pH variation occurred during the runs. All kinetic runs were performed up to ca. 70% substrate degradation and repeated at least twice, to check their reproducibility.

3. Results and discussion

3.1. Photocatalysts physical properties

As shown in Table 1, BET analysis evidenced that materials containing small W amounts have slightly larger surface area with respect to the reference T sample, in agreement with smaller anatase crystallite nanoparticles calculated from XRPD spectra. The W material, crystallized in the monoclinic WO$_3$ phase, showed instead a very low SSA of 3.8 m^2 g^{-1}.

The pore size distribution of the investigated mixed oxides, obtained by the Barrett–Joyner–Halenda (BJH) analysis of the N$_2$ desorption isotherms and reported in Fig. 1, reveals a mesoporous structure, mainly in the small (2–5 nm) and medium (5–20 nm) size ranges, similar for all the investigated materials. However, T_W(X) samples exhibit a lower content of relatively large pores (20–50 nm of diameter) with respect to the corresponding T material.

The UV–vis absorption spectra of the investigated photocatalyst materials are shown in Fig. 2. The pure WO$_3$ sample exhibits an absorption onset at ∼460 nm, in line with the band-gap value of 2.7–2.8 eV reported for this material in the monoclinic phase [27–29]. All T_W(X) samples have a similar absorption threshold around 400 nm, typical of the anatase phase; an extra absorption contribution in the 400–500 nm region is observed for T_W(X) with increasing the nominal W content. The visible light absorption shoulder, particularly evident in the absorption spectrum of

Table 1

Specific surface area (SSA) from BET analysis and results of Rietveld refinements of XRPD patterns, assuming the absence of amorphous materials: weight fraction of crystalline WO_3; a and c cell parameters and z coordinate of O-site description for the anatase unit cell; calculated TiO_2 anatase particles size (d_A).

Sample	SSA ($m^2\,g^{-1}$)	h-WO_3 (wt.%)	Anatase phase			
			a (Å)	c (Å)	z(O)	d_A (nm)
T	64	–	3.78758(5)	9.5051(2)	0.1664(1)	11.8(6)
T_W(0.2)	72	–	3.78847(8)	9.5005(2)	0.1661(1)	8.6(5)
T_W(0.5)	77	–	3.78903(8)	9.5004(2)	0.1663(1)	9.2 (5)
T_W(1)	73	0.05(2)%	3.78974(8)	9.4996(2)	0.1660(1)	9.8(7)
T_W(3)	65	0.3(1)%	3.79184(8)	9.4985(2)	0.1661(1)	11.0(7)
T_W(5)	80	0.7(1)%	3.7933(1)	9.4883(3)	0.1656(1)	8.4(9)
T_600	–	–	3.78722(5)	9.5083(2)	0.16666(6)	15.3(8)
T_W(5)_600	–	0.9(1)%	3.78993(5)	9.5008(2)	0.16664(6)	15.5(9)

Fig. 3. High resolution XPS spectra in the W 4d BE region of WO_3 and T_W(X) samples.

Table 2

Atomic ratios relative to Ti atoms obtained from the XPS analysis of selected photocatalysts.

Sample	W/Ti (%)	O/Ti	K/Ti
T	–	1.98	0.17
T_W(1)	4.9	1.97	0.18
T_W(3)	14.6	2.15	0.17
W	–	2.80	

4f signal with the Ti 3p signal. The W/Ti atomic ratios calculated by this way, 4.9% and 14.6% for T_W(1) and T_W(3), respectively, confirm the expected relative W content in the two samples, though being much higher than the nominal values, in line with previous results for similar materials [20].

The XPS spectra of the two T_W(X) systems in terms of both shape and BE positions perfectly resemble the doublet peaks of the W sample (WO_3 powder reference, see Fig. 3), thus confirming the presence of full oxidized tungsten, which may be segregated in nanometric WO_3 clusters coupled to TiO_2 or partially included in the anatase phase.

Surprisingly, almost identical O 1s spectra with a main peak centered at 530.2 eV, typical of oxygen in the TiO_2 lattice, and a shoulder at higher BE (531.6 eV), which can be assigned to surface hydroxyl groups [32], are shown by all TiO_2-containing samples (see Fig. 4a). In particular, the deconvolution procedure applied to the O 1s XPS signal of each sample and the relative percent contribution of the less intense −OH component are included in Fig. 4b. With increasing the nominal W content also the O/Ti atomic ratios calculated from XPS analysis slightly increased, as reported in Table 2, in line with the expected segregation of WO_3 clusters on the TiO_2 surface. Furthermore, based on the O 1s XP spectra shown in Fig. 4, with increasing WO_3 amount the surface hydroxylation seems to slightly decrease without any marked effect on the chemical environment of oxygen atoms, supporting the hypothesis of the formation of isolated WO_3 nanodomains rather than that of TiO_2 doping with tungsten.

Finally, the XPS survey analysis evidences the presence of the K 1s signal (~5 at.%), arising from the KOH aqueous solution employed in the sol-gel synthesis of amorphous P TiO_2. As shown in Table 2, very similar amounts of K were detected in all investigated samples, which potentially affect their surface properties in the same way and stabilize tiny WO_3 nanoclusters in the hexagonal phase dispersed onto the TiO_2 surface, evidenced by XRPD analysis. XP spectra do not show the N 1s peak for both T_W samples, ruling out the presence of surface N-containing species, within the sensitivity of XPS analysis.

EDX analysis confirmed the W nominal amount assessed in the synthesis procedure. In particular W/Ti atomic ratios equal to (1.05 ± 0.23)%, (3.38 ± 0.2)% and (5.57 ± 0.54)% were found for T_W(1), T_W(3) and T_W(5), respectively.

T_W(5), can be due to WO_3 aggregates or to the presence of N-containing species originated from the here employed W precursor and not completely removed by annealing at 450 °C.

This hypothesis is confirmed by a comparison between the absorption spectrum of T_W(5) and that of T_W(5)_600 containing the same nominal W amount as T_W(5) but calcined in air at 600 °C, instead of 450 °C. Earlier investigation on N-containing TiO_2 photocatalytic materials [30,31] showed that almost complete removal of nitrogen species, usually encapsulated in micro-voids or differently trapped in the bulk of TiO_2 systems, is guaranteed by annealing at high temperature. As shown in the inset of Fig. 2, the absorption response of T_W(5)_600 in the 400–500 nm range is lower than that of T_W(5), though T_W(5)_600 retains a slightly higher visible light absorption with respect to full anatase T, resembling the typical absorption of WO_3 in hexagonal phase [28]. This confirms that the enhanced visible light absorption shown by T_W(X) mixed oxides with relatively high W loading and calcined at 450 °C can be attributed to both N-containing species and WO_3 domains.

The surface composition of selected samples was investigated by XPS. In particular, we focused on T_W(1) and T_W(3) in comparison to pure TiO_2 (T) or WO_3 (W). First of all, almost identical Ti 2p doublet signals (not shown), with two components at binding energy (BE) 464.7 and 459.0 eV, assigned to Ti $2p_{1/2}$ and Ti $2p_{3/2}$, respectively, were recorded with both T and TiO_2-WO_3 mixed oxides.

For W analysis we considered the W 4d binding region (see Fig. 3), instead of the 4f core levels, due to the superposition of the W
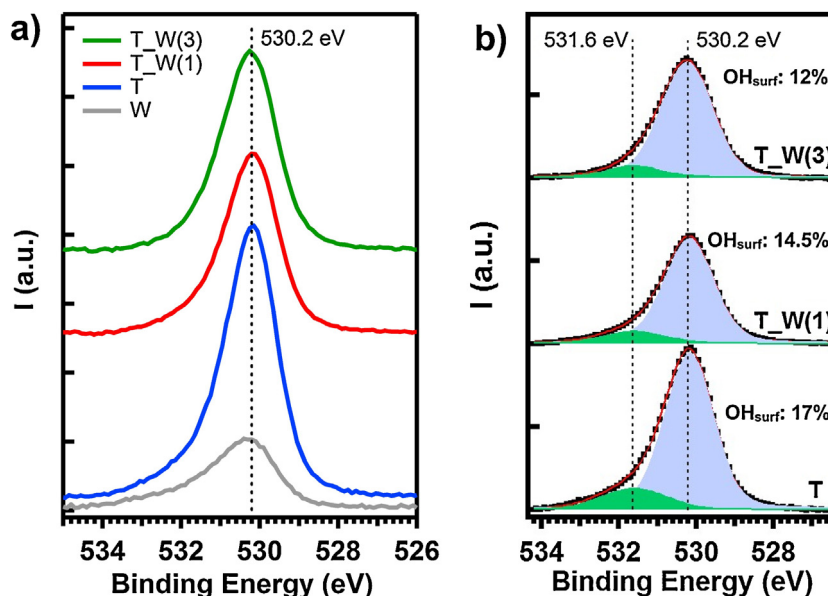
Fig. 4. (a) Comparison of O 1s XPS spectra of pure WO_3, TiO_2 and T_W(X) mixed oxides. (b) Deconvolution of O 1s spectra, showing the relative contributions of surface hydroxyl groups (OH_{surf}) and oxygen in the TiO_2 lattice (green and light blue area, respectively). (For interpretation of the references to color in this figure legend, the reader is referred to the web version of this article.)
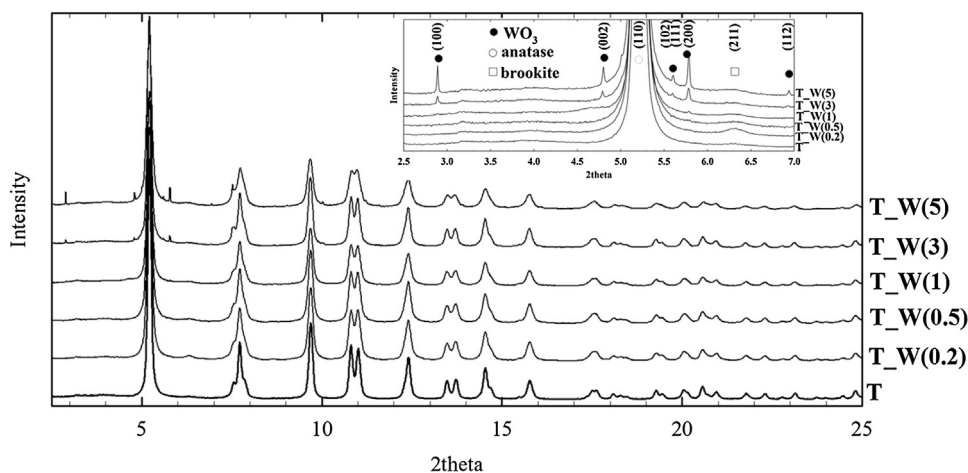

Fig. 5. Experimental XRPD patterns of the TiO_2-WO_3 samples calcined at 450 °C. The inset highlights the 2.5–7.0° 2θ range, with the characteristic reflections of WO_3 (full circles) and of TiO_2 brookite (void square).

3.2. Photocatalysts structure by XRPD analysis

The experimental XRPD patterns obtained with the mixed oxide powders calcined at 450 °C are shown in Fig. 5, while the low intensity profile recorded in the 2.5–7.0° 2θ range is highlighted in the inset of Fig. 5. All samples contain anatase as the main crystallographic phase, as demonstrated by the reflection at 2θ = 25.4° due to the (1 0 1) reflection of anatase. They also contain ∼5-10% of brookite, as testified by the bump in the traces background at 2θ around 6.3° (d ∼ 2.9 Å). The very broad feature of this main brookite reflection suggests that brookite nanoparticles are very small in size and also prevent an accurate determination of the brookite phase fraction. No evidence of the presence of rutile is observed in any sample.

In addition to those due to TiO_2 phases, other reflections appear in the XRPD patterns and become more marked with increasing W/Ti ratio, as shown in the inset of Fig. 5. These signals are fingerprints of the WO_3 hexagonal phase (hereafter h-WO_3), characterized by a $P6_3/mcm$ space group. In the specific case of the

T_W(5)_600 sample, the a and c lattice parameters are 7.3088(4) Å and 7.6696(6) Å, respectively.

On the other hand, reference pure WO_3 exhibits a single monoclinic phase, as generally reported in the literature [33]. The hexagonal phase of WO_3 is reported to be stabilized by intercalation of other chemical species, generally in the form of monovalent cations, such as ammonium [34,35], alkaline (Li, Na, K) [34,36] or even heavy metal (Tl, In, Pb) ions [36,37].

Both NH_4^+ and K^+ ions, deriving from the ammonium metatungstate hydrate and KOH precursors, respectively, may be responsible for the stabilization of h-WO_3 in T_W(X) samples. The inclusion of both of them is reported to produce similar effects on the h-WO_3 cell parameters, close to those observed in this study. Conversely, attempts to produce pure h-WO_3 by dehydration of $WO_3 \cdot 1/3H_2O$ led to a much larger c-axis (∼7.8–7.9 Å) [34,38].

The observed thermal stability of h-WO_3 suggests the inclusion of K^+, since h-WO_3 with ammonium inclusions was reported to decompose above ∼500 °C transforming h-WO_3 into the monoclinic phase [36]. Moreover, pure WO_3 prepared starting from a

NH_4^+-containing W precursor (in the absence of KOH solution) showed a monoclinic cell, indirectly confirming that h-WO_3 in T_W(X) is principally stabilized by intercalation of K^+, rather than by NH_4^+.

Concerning quantitative phase analysis, the weighted phase fractions reported in Table 1 were calculated by assuming a $K_{0.32}W_{0.95}O_3$ composition of surface tungsten-containing domains, corresponding to the solubility limit of K^+ into WO_3, as expected in the presence of an excess of K^+. The calculated cell parameters match well the tabulated ones [36].

Traces of WO_3 were noticed only in T_W(5) and T_W(5)_600 when employing a laboratory XRPD source. However, the high brilliance of the ID22 beamline at ESRF allowed to attain a very high signal to noise ratio, thus improving the sensitivity of quantitative phase analysis, as clearly evidenced in Fig. 5.

The crystallite size of the anatase phase, calculated through the Williamson-Hall method [39], are listed in Table 1. The use of small amounts of W precursor, combined with calcination at 450 °C, ensured the formation of anatase nanoparticles with size of *ca.* 9–10 nm, *i.e.* relatively smaller than those of reference T sample. However, the progressive increase of W content produced a slight particle size enlargement, the only exception to this trend being the T_W(5) sample. Upon sintering at higher temperature, the anatase crystals grew to ~16 nm.

Pure monoclinic WO_3 showed particles size in the order of hundreds of nanometers. In the case of the brookite phase, particle sizes around 5 nm were evaluated for all TiO_2-containing samples by means of the Scherrer formula, only the first, broad reflection of brookite being detectable.

As shown in Table 1, the *a* cell parameter of the tetragonal anatase increases monotonically with the W/Ti ratio, in line with literature reports [40–42]. This behavior can be related to the substitution of W^{+6} for Ti^{+4}. The slightly smaller ionic radius of W^{+6} compared to that of Ti^{+4} [43] may be counterbalanced by Ti^{+4} vacancies to allow for electroneutrality. This structural modification, energetically more favorable with respect to the alternative inclusion of oxygen at interstitial positions [41], was proposed to explain the expansion of the *a* cell parameter in $TiO_{2+\delta}$ materials [44].

Conversely, the *c* cell axis shrinks with increasing the W amount, also in line with previous findings [40]. However, an opposite behavior was observed by Fernández-García *et al* [41]. Whereas Kim *et al* [42] noticed a contraction of the *c*-axis only above a critical W concentration value. The competitive inclusion of other non-metal elements, such as N-containing species, originated by the here employed N-containing W precursor, and not completely removed by annealing at 450 °C [31,45] may be responsible for this effect. This was verified by considering the cell parameters of the same materials sintered at 600 °C, which retain the same phase composition.

As reported in Table 1, T_W(5)_600 exhibits expansion of *a* and contraction of *c* with respect to T_600, though these effects, to be related in this case to the presence of W only, are much less evident when compared to the same material sintered at 450 °C. Therefore, the values of the unit cell parameters of the materials calcined at 450 °C are likely to be affected by N-containing species, besides by W, which remains the main additional component in the coupled systems, even after calcination at 600 °C.

The evolution of the *z*(O) coordinate of the anatase unit cell, describing the O apical position in TiO_6 octahedra, may better elucidate the changes induced on the anatase structure by WO_3 addition to TiO_2. This parameter is particularly sensitive to the defects related to O (non metal) ions, such as oxygen vacancies, inclusion of N-containing species, etc. As reported in Table 1, *z*(O) decreases monotonically with increasing the W/Ti ratio in samples calcined at 450 °C. However, such effect vanishes after calcination at
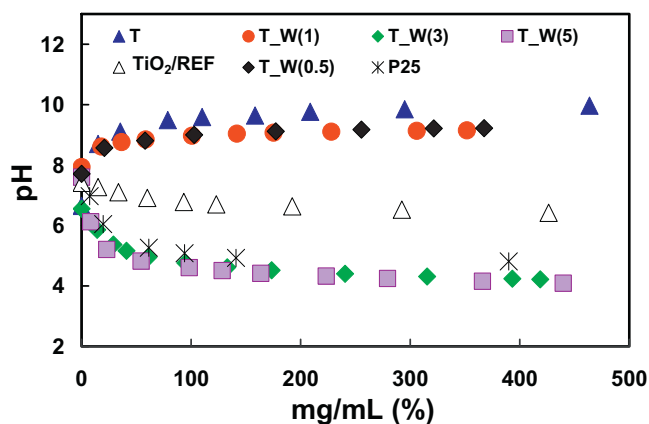

Fig. 6. pH$_{pzc}$ evaluation of TiO_2-WO_3 samples by the mass titration method. Pure TiO_2 (TiO_2/REF) prepared by a standard sol-gel method and commercial Aeroxide® TiO_2 P25 are also included for comparison.

600 °C, suggesting that high temperature treatment removes most of the nitrogen-containing species from the anatase structure. Thus, W inclusion into anatase should account for the variation of the cell parameters after calcination at 600 °C.

The estimated fraction of crystalline WO_3 increases with the W content, reaching a maximum value of ~0.9 wt.% (~0.4 at.%) for T_W(5)_600, which still remains below the nominal value. This suggests that upon heat treatment a fraction of tungsten may migrate into the TiO_2 structure (by substituting Ti atoms) or just remains in the form of amorphous WO_x, as recently reported [46]. In fact, the h-WO_3 fraction reported in Table 1 accounts for crystalline WO_3 only, while the presence of small amounts of amorphous WO_x cannot be excluded. On the other hand, the W/Ti occupation fraction of crystalline anatase, estimated by Rietveld refinement, turned out to be not-negligible, *i.e.* around 1–2 at.%, only for T_W(3), T_W(5) and T_W(5)_600.

In conclusion, XRPD analysis evidences partial segregation crystalline WO_3 in hexagonal phase in T_W(X) samples, with grain size much larger than that of anatase, and that a small W fraction, up to ~2 at.%, is likely to enter the anatase phase.

3.3. pH$_{pzc}$ characterization

The pH$_{pzc}$ results obtained by applying the mass titration method are shown in Fig. 6. The titration curves obtained with a TiO_2 sample (TiO_2/REF), prepared by following a standard sol-gel procedure [31], and with commercial Aeroxide® TiO_2 P25 are also reported for comparison.

First of all, the pH plateau value of the T sample (~9.9) is surprisingly high with respect to the pH$_{pzc}$ of TiO_2, between 3.5 and 6.5, reported in literature [47] and also with respect to the value obtained with reference P25 (~4.8). This is due to the presence of K^+ ions on the oxide surface, detected by XPS analysis, which could be involved in an ionic exchange with H^+ species in the electrolyte solution [48]. With increasing the W amount in the mixed oxides a progressive decrease of the pH plateau value is observed, the lowest pH$_{pzc}$ value of ~4.5 being achieved with T_W(5). This is an indirect evidence of the progressive enrichment in WO_3 super-acidic domains of the TiO_2 surface [49].

Nevertheless, all pH$_{pzc}$ values are higher than the pH (3.5–3.7) of the photocatalytic test reactions. Thus, the surface of all photocatalysts is expected to be positively charged and consequently able to adsorb the investigated model pollutants, both being in anionic form.
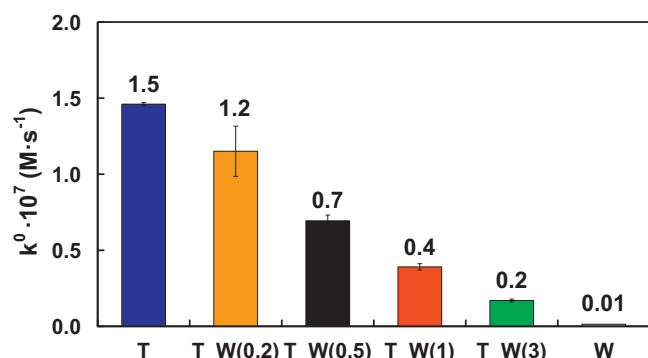
Fig. 7. Zero order rate constants of formic acid photomineralization under UV–vis irradiation in the presence of the investigated photocatalysts (0.1 g L^{-1}).

Fig. 8. Photocatalytic reduction of Cr(VI) ions in the presence of the investigated photocatalysts (0.1 g L^{-1}).

3.4. Photocatalytic activity

3.4.1. Photocatalytic oxidation reaction

FA photocatalytic degradation occurred at a constant rate, *i.e.* according to a zero order rate law, as in previous studies [3,4,25,30,50,51]. Therefore, the activity of the here investigated TiO$_2$-based materials in FA photocatalytic oxidation can be compared in terms of zero order rate constants $k°$, as shown in Fig. 7.

Firstly, we observed that the maximum FA decomposition rate, quite similar to that obtained in the presence of the same amount of commercial P25 TiO$_2$ ($k°\cdot10^7 = 1.49 \pm 0.02$ M s^{-1}), is achieved with the home-made T sample.

Nevertheless, the photocatalytic activity in this reaction monotonously decreased with increasing X in T_W(X) oxide photocatalysts, attaining an extremely low value with pure WO$_3$. As FA photocatalytic mineralization mainly proceeds via its direct interaction with photoproduced holes [52], the observed photoactivity decrease might be related to a hampered adsorption of formate anions on the T_W(X) surface. However, by considering that the point of zero charge (pH$_{pzc}$) of our home-made materials, containing residual traces of K$^+$, appears surprisingly high, *i.e.* at pH 10 and 4 for T and T_W(5) respectively (Fig. 6), in the 3.5–3.7 pH range of this reaction the affinity of formate anions for the positively charged T_W(X) surfaces is not expected to be suppressed. On the other hand, the data reported in Fig. 7 clearly evidence that W addition to the TiO$_2$-based photocatalysts *per se* negatively affects their photoactivity properties in this oxidation reaction. This fact may be related to the progressive, though slight, reduction of surface hydroxylation with increasing W/Ti ratio, as evidenced by XPS analysis (Fig. 4b), which may affect the adsorption of the substrate on TiO$_2$-WO$_3$ mixed oxides [20].

A more sound explanation of the observed photocatalytic behavior is associated to the electronic structure of the materials, and in particular to the positions of the CB and VB edges of the TiO$_2$ and WO$_3$ semiconductors, in relation to the redox potentials of the reaction substrate adsorbed on the photocatalyst surface. In fact, according to the usually accepted activation mechanism of TiO$_2$-WO$_3$ systems [13,53], photopromoted electrons can be transferred from the CB of TiO$_2$ to the CB of coupled WO$_3$, which are located at −0.16 and +0.15 V *vs.* NHE (pH 0), respectively, with the consequent formation of W^{5+} centers, while photogenerated holes might be trapped within the TiO$_2$ particles. In the case of photocatalytic oxidation reactions, such as FA decomposition under aerobic conditions, photo-excited CB electrons are usually scavenged by molecular oxygen at the anatase TiO$_2$ surface, where one-electron reduction of O$_2$ occurs. However, as the O$_2$/HO$_2$• reduction potential is −0.046 V *vs.* NHE (pH 0), the electron transfer to molecular oxygen on the surface of T_W(X) photocatalysts is expected to be slower compared to that occurring in T (pure
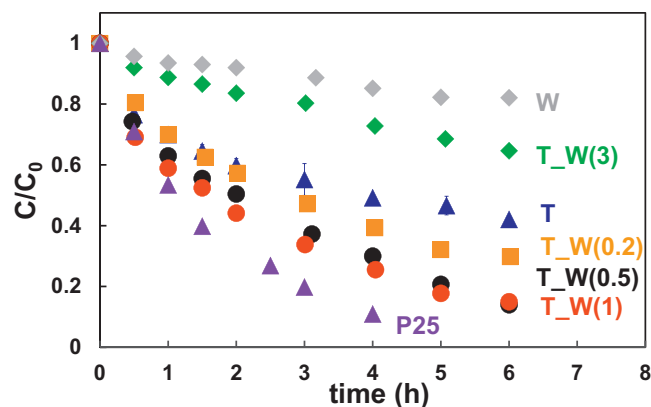
TiO$_2$) [54], because of the lower reduction power of the electrons transferred in the CB of WO$_3$ (located at +0.15 V *vs.* NHE), with a consequent decreased formation of superoxide radical anion O$_2^{-•}$. Photopromoted electrons thus remain within the TiO$_2$-WO$_3$ hybrid system and may easily undergo recombination with photoproduced holes [55]. This explains the observed photoactivity decrease in FA photo-mineralization with increasing the relative W/Ti content in the presence of WO$_3$ domains on the TiO$_2$ surface.

3.4.2. Photocatalytic Cr(VI) reduction

The effects induced by modifying TiO$_2$ with different amounts of WO$_3$ was investigated also in the photocatalytic reduction of Cr(VI). Such common pollutant of waste waters, usually present in the form of highly soluble and toxic chromate anions, is photocatalytically converted into Cr(III), which exhibits lower toxicity and mobility in the environment [56,57]. This process is possible on the grounds of the energy level of the TiO$_2$ CB and of the reduction potential of the Cr(VI)/Cr(III) couple and it is favored at low pH, because the redox potential of Cr(VI)/Cr(III) couple, involving the transfer of three electrons, with decreasing pH shifts to more positive values with a slope higher than that of the CB edge shift with pH [58].

The results of Cr(VI) photocatalytic reduction carried out with T_W(X) samples and commercial P25 TiO$_2$ are compared in Fig. 8. In this case coupling TiO$_2$ with WO$_3$ was beneficial in increasing the overall reaction rate and a volcano-shaped photoactivity trend was obtained. In particular, T_W(1) exhibits the highest photocatalytic activity, approaching that attained with P25, whereas over-loading of WO$_3$ domains clearly produced a decrease of the photocatalytic efficiency (see the results obtained with T_W(3) in Fig. 8).

Thus, a different photoactivity trend of T_W(X) materials was clearly outlined in the two investigated test reactions, though both occurred in the same pH range under intentionally chosen similar substrate-photocatalyst electrostatic interactions.

In fact, small amounts of WO$_3$ (0.2–1.0 mol%) produced beneficial effects in the photoreduction of Cr(VI) ions (Fig. 8). As already mentioned, WO$_3$ domains on the TiO$_2$ surface can act as an acceptor of photopromoted CB electrons, with a consequently increased efficiency of charged carriers separation, since W(VI) can be easily reduced to W(V). The here employed synthetic route seems to ensure an intimate and efficient coupling between the two oxides leading to a fruitful exploitation of the well-known electron storage capability of WO$_3$ [54,59] under the investigated conditions.

Notably, photopromoted electrons transferred from the CB of TiO$_2$ to the CB of coupled WO$_3$ are in this case energetically able to efficiently reduce the adsorbed Cr(VI) species, the CB of WO$_3$ and the redox potential of the Cr(VI)/Cr(III) being located at ∼0 and +1 V
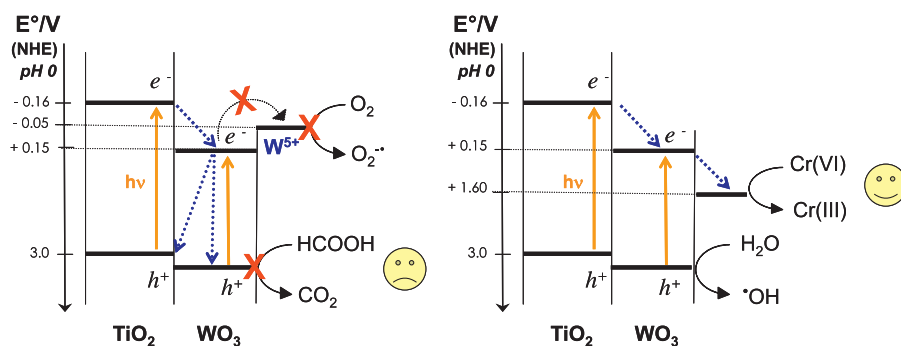
Scheme 1. Electron transfer paths at work in the TiO$_2$-WO$_3$ mixed oxides with WO$_3$ domains on the TiO$_2$ surface, based on the conduction and valence band edges of the single semiconductors, in relation to the redox potentials of the electron acceptor species directly (or indirectly) involved in the examined photocatalytic processes.

vs. RHE (at pH 3.7), respectively. Furthermore, the slightly higher SSA of the T_W(X) materials with respect to pure TiO$_2$ may also contribute in increasing their photoactivity.

Thus, as shown in Scheme 1, the electron scavenging power of WO$_3$ domains on the TiO$_2$ lattice may produce a different photoactivity response, strongly depending on the redox potential of the electron acceptor species involved in the examined photocatalytic process. In particular under irradiation in aerobic conditions, the electrons transferred from TiO$_2$ CB and trapped as W^{5+} sites cannot be efficiently transferred to O$_2$ molecules because of the unfavorable matching of the CB edge of WO$_3$ with the redox potential of the O$_2$/O$_2^{-\bullet}$ couple. They thus competitively recombine with the photogenerated holes, which therefore are no longer available for FA molecules oxidation, with a consequent drop of the overall photocatalytic activity of the mixed oxides materials with respect to pure TiO$_2$.

Conversely, when operating under aerobic conditions in the presence of an electron acceptor species with a redox potential more positive (on the electrochemical scale) than the CB edge of WO$_3$, *e.g.* Cr$_2$O$_7^{2-}$ anions, the electrons accumulated on WO$_3$ domains may be efficiently transferred to that species inducing its reduction, while photoproduced holes may be involved in H$_2$O molecules oxidation with OH radicals production. In this second case the beneficial effects on promoting charge carriers separation induced by coupling TiO$_2$ with WO$_3$ domains may be fruitfully exploited in photocatalysis and account for the better performance of TiO$_2$-WO$_3$ mixed oxides with respect to pure TiO$_2$ in photocatalytic Cr(VI) reduction.

Finally, as T_W(1) was the best performing photocatalyst in Cr(VI) photoreduction, a 1% W/Ti molar ratio corresponds to the optimum tungsten content guaranteeing TiO$_2$ coupling with a proper WO$_3$ amount, without producing a too marked distortion of the TiO$_2$ anatase cell. Over-loading TiO$_2$ with WO$_3$ aggregates produces a decrease of photocatalytic efficiency, possibly due to an increased extent of structural defects in the anatase structure which may act as e$^-$/h$^+$ pairs recombination centers.

4. Conclusions

Smaller anatase nanoparticles were formed upon addition of small amounts of tungsten to titania, with slightly larger SSA with respect to pure TiO$_2$, in line with the tungsten ability of inhibiting the anatase crystal growth, and this might contribute to the higher photocatalytic activity of TiO$_2$/WO$_3$ materials. Furthermore, though most of tungsten remained in oxide form on the photocatalyst surface, the here adopted synthesis method allowed for tungsten migration within the TiO$_2$ lattice during annealing, as demonstrated by the progressive distortion of the anatase cell with increasing the W content in TiO$_2$.

WO$_3$ domains on the surface of anatase TiO$_2$ photocatalysts ensure better photoproduced charge separation by electron transfer from the CB of TiO$_2$ to the CB of WO$_3$. However, the transferred electrons are not able to reduce adsorbed oxygen, and mainly recombine with photoproduced holes, thus resulting in a progressive decrease in the rate of FA mineralization with increasing the amount of tungsten oxide added to TiO$_2$ photocatalysts. On the other hand, such electrons trapped in WO$_3$ are able to reduce Cr(VI) species, with an increased rate of bichromate reduction under aerobic conditions. This demonstrates efficient photopromoted electron transfer from TiO$_2$ to WO$_3$ in our TiO$_2$/WO$_3$ coupled system, leading to better electron-hole separation. This results in increased photocatalytic activity only in the presence of electron acceptor species, such as dichromate anions, with a redox potential lower in energy than the CB edge of WO$_3$.

Acknowledgments

References

[1] S.G. Kumar, L.G. Devida, J. Phys. Chem. A 115 (2011) 13211–13241.
[2] H. Park, Y. Park, W. Kim, W. Choi, J. Photochem. Photobiol. C: Photochem. Rev. 15 (2013) 1–20.
[3] M.V. Dozzi, L. Prati, P. Canton, E. Selli, Phys. Chem. Chem. Phys. 11 (2009) 7171–7180.
[4] M.V. Dozzi, A. Saccomanni, M. Altomare, E. Selli, Photochem. Photobiol. Sci. 12 (2013) 595–601.
[5] M. Dahl, Y. Liu, Y. Yin, Chem. Rev. 114 (2014) 9853–9889.
[6] T. Ivanova, A. Harizanova, T. Koutzarova, B. Vertruyen, J. Non-Cryst. Solids 357 (2011) 2840–2845.
[7] X.Z. Li, F.B. Li, C.L. Yang, W.K. Ge, J. Photochem. Photobiol. A: Chem. 141 (2001) 209–217.
[8] N. Couselo, F.S. García Einschlag, R.J. Candal, M. Jobbágy, J. Phys. Chem. C 112 (2008) 1094–1100.
[9] O. Lorret, D. Francova, G. Waldner, N. Stelzer, Appl. Catal. B: Environ. 91 (2009) 39–46.
[10] Y.T. Kwon, K.Y. Song, W.I. Lee, G.J. Choi, Y.R. Do, J. Catal. 191 (2000) 192–199.
[11] B. Tryba, M. Piszcz, A.W. Morawski, Intern. J. Photoenergy (2009), Article ID 297319.
[12] S. Liu, J. Huang, L. Cao, J. Li, H. Ouyang, X. Tao, C. Liu, Mater. Sci. Semicond. Process. 25 (2014) 106–111.
[13] C. Shifu, C. Lei, G. Shen, C. Gengyu, Powder Technol. 160 (2005) 198–202.
[14] K.K. Akurati, A. Vital, J.-P. Dellemann, K. Michalow, T. Graule, D. Ferri, A. Baiker, Appl. Catal. B: Environ. 79 (2008) 53–62.
[15] A.M. Cant, F. Huang, X.L. Zhang, Y. Chen, Y.-B. Cheng, R. Amal, Nanoscale 6 (2014) 3875–3880.
[16] X. Qu, D. Xie, L. Gao, L. Cao, F. Du, J. Mater. Sci. 50 (2015) 21–27.
[17] A.O.T. Patrocinio, L.F. Paula, R.M. Paniago, J. Freitag, D.W. Bahnemann, ACS Appl. Mater. Interfaces 6 (2014) 16859–16866.
[18] B. Ohtani, J. Photochem. Photobiol. C: Photochem. Rev. 11 (2010) 157–178.
[19] H. Kim, J. Kim, W. Kim, W. Choi, J. Phys. Chem. C 115 (2011) 9797–9805.

[20] F. Riboni, L.G. Bettini, D.W. Bahnemann, E. Selli, Catal. Today 209 (2013) 28–34.

[21] A.C. Larson, R.B. Von Dreele, General Structural Analysis System (GSAS); Los Alamos National Laboratory Report LAUR 86748; Los Alamos, NM, 2004.

[22] N.N. Lobanov, L. Alte da Veiga, 6th European Powder Diffraction Conference 1998, 12–16.

[23] G.K. Williamson, W.H. Hall, Acta Metall. 1 (1953) 22–31.

[24] J.S. Noh, J.A. Schwarz, J. Colloid Interface Sci. 130/1 (1989) 157–164.

[25] M.V. Dozzi, A. Saccomanni, E. Selli, J. Hazard. Mater. 211 (2012) 188–195.

[26] L.S. Clesceri, A.E. Greenberg, A.D. Eaton (Eds.), Standard Methods for the Examination of Water and Wastewater, 20th ed., American Public Health Association, Washington, DC, 1998.

[27] G.R. Bamwenda, K. Sayama, H. Arakawa, J. Photochem. Photobiol. A 122 (1999) 175–183.

[28] S.S. Kalanur, Y.J. Hwang, S.Y. Chae, O.H. Joo, J. Mater. Chem. A 1 (2013) 3479–3488.

[29] I. Grigioni, K.G. Stamplecoskie, E. Selli, P.V. Kamat, J. Phys. Chem. C 119 (2015) 20792–20800.

[30] M.V. Dozzi, S. Livraghi, E. Giamello, E. Selli, Photochem. Photobiol. Sci. 10 (2011) 343–349.

[31] M.V. Dozzi, B. Ohtani, E. Selli, Phys. Chem. Chem. Phys. 13 (2011) 18217–18227.

[32] L. Artiglia, A. Zana, G.A. Rizzi, S. Agnoli, F. Bondino, E. Magnano, E. Cavaliere, L. Gavioli, G. Granozzi, J. Phys. Chem. C 116 (2012) 12532–12540.

[33] A. Kubacka, A. Iglesias-Juez, M. di Michiel, A.I. Becerro, M. Fernández-García, Phys. Chem. Chem. Phys. 16 (2014) 19540–19549.

[34] K.H. Cheng, A.J. Jacobson, M.S. Whittingham, Solid State Ionics 5 (1981) 335–358.

[35] M. Szilàgyi, L. Wang, P.-I. Gouma, C. Balàzsi, J. Madaràsz, G. Pokol, Mater. Res. Bull. 44 (2009) 505–508.

[36] T. Kudo, J. Oi, A. Kishimoto, M. Hiratani, Mater. Res. Bull. 26 (1991) 779–787.

[37] P. Labbé, M. Goreaud, B. Raveau, J.C. Monier, Acta Cryst. B 34 (1978) 1433–1438.

[38] B. Gerand, G. Nowogrocki, J. Guenot, M. Figlarz, J. Solid State Chem. 29 (1979) 429–434.

[39] G.K. Williamson, W.H. Hall, Acta Metall. 1 (1953) 22–31.

[40] A. Fuerte, M.D. Hernández-Alonso, A.J. Maira, A. Martinez-Arias, M. Fernández-García, J.C. Conesa, J. Soria, G. Munuer, J. Catal. 212 (2002) 1–9.

[41] M. Fernández-García, A. Martinez-Arias, A. Fuerte, J.C. Conesa, J. Phys. Chem. B 109 (2005) 6075–6083.

[42] D.-S. Kim, J.-H. Yang, S. Balaji, H.-J. Cho, M.-K. Kim, D.-U. Kang, Y. Djaoued, Y.-U. Kwon, CrystEngComm 11 (2009) 1621–1629.

[43] D. Shannon, Acta Crystallogr. A 32 (1976) 751–767.

[44] V. Etacheri, M.K. Seery, S.J. Hinder, S.C. Pillai, Adv. Funct. Mater. 21 (2011) 3744–3752.

[45] M.V. Dozzi, E. Selli, J. Photochem. Photobiol. C: Photochem. Rev. 14 (2013) 13–28.

[46] M. Epifani, R. Dìaz, C. Force, E. Comini, M. Manzanares, T. Andreu, A. Genç, J. Arbiol, P. Siciliano, G. Faglia, J.R. Morante, ACS Appl. Mater. Interfaces 7 (2015) 6898–6908.

[47] J.P. Jolivet, M. Henry, J. Livage, Metal Oxide Chemistry and Synthesis, Wiley, New York, 2000.

[48] Y. Bessekhouad, D. Robert, J.-V. Weber, N. Chaoui, J. Photochem. Photobiol. A 167 (2004) 49–57.

[49] M.A. Saepurahman, F.K. Abdullah, F.K. Chong, J. Hazard. Mater. 176 (2010) 451–458.

[50] C. Bernardini, M.V. Dozzi, G. Cappelletti, E. Selli, J. Photochem. Photobiol.: Chem. 211 (2010) 185–192.

[51] M.V. Dozzi, G.L. Chiarello, E. Selli, J. Adv. Oxid. Technol. 13 (2010) 305–312.

[52] M. Mrowetz, E. Selli, New J. Chem. 30 (2006) 108–114.

[53] J.A. Rengifo-Herrera, M.N. Blanco, L.R. Pizzio, Appl. Catal. B: Environ. 110 (2011) 126–132.

[54] D. Zhao, C. Chen, C. Yu, W. Ma, J. Zhao, J. Phys. Chem. C 113 (2009) 13160–13165.

[55] Y. Liu, C. Xie, J. Li, T. Zou, D. Zeng, Appl. Catal. A: Gen. 4333–434 (2012) 81–87.

[56] V. Bianchi, A. Zantedeschi, A. Montaldi, J. Majone, Toxicol. Lett. 8 (1984) 279–286.

[57] S. Music, M. Ristic, M. Tonkovic, Z. Wasser Abwass, Forsch 19 (1986) 186–196.

[58] X. Wang, S.O. Pehkonen, A.K. Ray, Ind. Eng. Chem. Res. 43 (2004) 1665–1672.

[59] T. Tatsuma, S. Saitoh, P. Ngaotrakanwiwat, Y. Ohko, A. Fujishima, Langmuir 18 (2002) 7777–7779.